



 Cite this: *RSC Adv.*, 2020, **10**, 29320

# From inverse sandwich $Ta_2B_7^+$ and $Ta_2B_8$ to spherical trihedral $Ta_3B_{12}^-$ : prediction of the smallest metallo-borospherene†

 Yu Zhang, Xiao-Yun Zhao, Miao Yan and Si-Dian Li \*

Transition-metal-doped boron nanoclusters exhibit interesting structures and bonding. Inspired by the experimentally discovered inverse sandwich  $D_{6h}$   $Ta_2B_6$  and spherical trihedral  $D_{3h}$   $La_3B_{18}^-$  and based on extensive first-principles theory calculations, we predict herein the structural transition from perfect di-metal-doped inverse sandwich  $D_{7h}$   $Ta_2B_7^+$  (1) and  $D_{8h}$   $Ta_2B_8$  (2) to tri-metal-doped spherical trihedral  $D_{3h}$   $Ta_3B_{12}^-$  (3). As the smallest metallo-borospherene reported to date,  $Ta_3B_{12}^-$  (3) contains three octa-coordinate Ta atoms as integral parts of the cage surface coordinated in three equivalent  $\eta^8$ - $B_8$  rings which share two eclipsed equilateral  $B_3$  triangles on the top and bottom interconnected by three  $B_2$  units on the waist. Detailed orbital and bonding analyses indicate that both  $Ta_2B_7^+$  (1) and  $Ta_2B_8$  (2) possess  $\sigma + \pi$  dual aromaticity, while  $Ta_3B_{12}^-$  (3) is  $\sigma + \pi + \delta$  triply aromatic in nature. The IR, Raman, and UV-vis or photoelectron spectra of the concerned species are computationally simulated to facilitate their future spectroscopic characterizations.

Received 25th June 2020

Accepted 31st July 2020

DOI: 10.1039/d0ra05570k

[rsc.li/rsc-advances](http://rsc.li/rsc-advances)

## 1. Introduction

Boron exhibits strong propensity to form multicentre-two-electron bonds (mc-2e bonds) in both polyhedral molecules and bulk allotropes due to its prototypical electron-deficiency.<sup>1–4</sup> Joint photoelectron (PE) spectroscopy experimental and first-principles theory investigations in the past two decades have unveiled a rich landscape for  $B_n^{-/0}$  boron nanoclusters from planar or quasi-planar structures ( $n = 3–38, 41–42$ ) to cage-like borospherenes ( $n = 39, 40$ ).<sup>3–7</sup> Cage-like  $D_{2d}$   $B_{40}^{-/0}$  are the first borospherenes discovered in 2014,<sup>5</sup> while  $C_3/C_2$   $B_{39}^-$  are the first axially chiral borospherenes confirmed in experiments as the global minima (GM) of the  $B_n^-$  monoanions.<sup>6</sup> These discoveries mark the onset of borospherene chemistry parallel to fullerene chemistry. The borospherene family has been systematically expanded by our group at first-principles theory levels to the cage-like  $B_n^q$  series in different charge states ( $n = 36–42, q = n–40$ ) which all possess twelve delocalized  $\pi$  bonds on the surface and follow the universal  $\sigma + \pi$  double delocalization bonding pattern.<sup>5–10</sup> Sea-shell-like  $C_2$   $B_{28}^{-/0}$  and  $C_s$   $B_{29}^-$  were later observed as minor isomers of the monoanions in PES experiments<sup>11,12</sup> and sea-shell-like  $C_s$   $B_{29}^+, C_2$   $B_{31}^+, C_2$   $B_{32}, C_2$   $B_{34}, C_2$   $B_{35}^+$ , and cage-like  $C_s$   $B_{39}^+$  have also been predicted recently in theory.<sup>13–16</sup>

Transition-metal (TM)-doping induces dramatic structural changes and leads to earlier planar  $\rightarrow$  tubular  $\rightarrow$  spherical structural transitions in boron clusters due to effective TM–B coordination interactions, as evidenced by the experimentally observed pyramidal  $C_{8v}$   $Ta@B_8^-$ ,<sup>17</sup>  $C_s$   $Ta@B_9^-$ ,<sup>18</sup> and perfect planar  $D_{10h}$   $Ta@B_{10}^-$  which has the highest coordination number of CN = 10 in planar species<sup>19</sup> and the theoretically predicted half-sandwich  $TaB_{12}^-$ .<sup>20</sup> A family of transition-metal-centred double-ring tubular boron complexes in staggered motifs were recently observed in experiments, including  $D_{8d}$   $Co@B_{16}^-$ ,<sup>21</sup>  $D_{9d}$   $Rh@B_{18}^-$ ,<sup>22</sup> and  $C_s$   $Ta@B_{20}^-$ ,<sup>23</sup> with  $C_s$   $Ta@B_{20}^-$  ( $B_2$ -[ $Ta@B_{18}^-$ ]) behaving like a tubular molecular rotor at 900 K facilitated by prototypical multicentre fluxional bonds (FBs) which form and break constantly.<sup>24</sup> A series of perfect di-metal-doped inverse sandwich complexes have also been observed in PE experiments, including  $D_{6h}$   $Ta_2B_6^{-/0}$ ,<sup>25</sup>  $D_{8h}$   $La_2B_8$ , and  $D_{8h}$   $Pr_2B_8$ .<sup>26</sup> Our group recently reported the smallest core-shell-like tubular molecular rotor  $C_{2h}$   $La_2[B_2@B_{18}]$  which contains a  $B_2$  core rotating inside a  $B_{18}$  tube almost freely.<sup>27</sup> The first experimentally observed tri-metal-doped inverse triple-decker  $C_{2v}$   $La_3B_{14}^-$  exhibits a tilted  $La-B_8-La-B_8-La$  triple-decker structure with two conjoined  $\eta^8$ - $B_8$  rings sharing a B–B unit on one edge.<sup>28</sup> With increasing cluster size, the first perfect spherical trihedral metallo-borospherenes  $D_{3h}$   $Ln_3B_{18}^-$  ( $Ln = La, Tb$ ) were very recently discovered in a joint PE experimental and first-principles theory investigation.<sup>29</sup> These metallo-borospherenes represent a new class of unusual geometry with tunable magnetic or catalytic properties, with three deca-coordinate Ln centres as integral parts of the cage surface coordinated in three equivalent  $\eta^{10}$ - $B_{10}$  decagons which share two eclipsed

Institute of Molecular Science, Shanxi University, Taiyuan, 030006, China. E-mail: [lisidian@sxu.edu.cn](mailto:lisidian@sxu.edu.cn)

† Electronic supplementary information (ESI) available. See DOI: 10.1039/d0ra05570k



triangular  $B_6$  units interconnected by three  $B_2$  units. Metallo-borospherenes were previously proposed in theory for  $MB_{40}$  ( $M = Be, Mg$ ) and  $Ni_nB_{40}$  ( $n = 1-4$ ) which contain hepta-coordinate metal centres on the cage surface of  $B_{40}$ , with the corresponding metallo-borophenes with hepta-coordinate metal centres as precursors.<sup>30,31</sup> However, it remains unknown at current stage what is the possible smallest size of metallo-borospherenes and if such coordination-stabilized metallo-borospherenes can be characterized in experiments.

Based on extensive first-principles theory calculations, we predict in this work the possibility of the perfect di-TM-doped inverse sandwich  $D_{7h}$   $Ta_2B_7^+$  (1) and  $D_{8h}$   $Ta_2B_8$  (2) and, more importantly, the smallest tri-TM-doped cage-like metallo-borospherene  $D_{3h}$   $Ta_3B_{12}^-$  (3) which contains three octa-coordinate Ta centres as integral parts of the cage surface coordinated in three equivalent  $\eta^8-B_8$  octagons that share two equilateral  $B_3$  triangles interconnected by three  $B_2$  units. Detailed analyses indicate that both  $Ta_2B_7^+$  (1) and  $Ta_2B_8$  (2) are  $\sigma + \pi$  dually aromatic in nature, while  $Ta_3B_{12}^-$  (3) is the first transition-metal-doped boron complex reported to date with  $\sigma + \pi + \delta$  triple aromaticity.

## 2. Theoretical procedure

Extensive global minimum (GM) searches were performed on  $Ta_2B_7^+$ ,  $Ta_2B_8$ , and  $Ta_3B_{12}^-$  using the Tsinghua Global Minimum (TGMin) package<sup>32,33</sup> based on a constraint Basin-Hopping algorithm,<sup>34</sup> with more than 2000 singlet or triplet stationary points explored for each cluster at PBE/DZVP level.<sup>35</sup> Low-lying isomers were then fully optimized at the PBE0 (36) level with the 6-311+G\* basis set<sup>37</sup> for B and Stuttgart relativistic small-core pseudopotential<sup>38,39</sup> for Ta using the Gaussian 16 program suite,<sup>40</sup> with vibrational frequencies checked to make sure that all isomers reported are true minima. The 15 lowest-lying isomers were subsequently fully re-optimized at both PBE0 and BP86 (ref. 41 and 42) levels with the basis sets of aug-cc-pVTZ for B<sup>43,44</sup> and Stuttgart+2f1g for Ta. Relative energies for the four lowest-lying isomers were further refined using the more accurate coupled cluster method with triple excitations CCSD(T)<sup>45-47</sup> implemented in Gaussian 16 with the same basis sets. Natural bonding orbital (NBO) analyses were performed using the NBO 6.0 program<sup>48</sup> and detailed bonding analyses carried out utilizing the adaptive natural density partitioning (AdNDP) approach.<sup>49,50</sup> Molecular dynamics (MD) simulations were performed on  $Ta_2B_7^+$  (1),  $Ta_2B_8$  (2), and  $Ta_3B_{12}^-$  (3) for 30 ps using the CP2K software suite at different temperatures.<sup>51</sup> The anisotropy of the current-induced density (ACID) analysis<sup>52</sup> was realized using the ACID code, with the ring-current maps generated using POV-Ray 3.7.<sup>53</sup> The iso-chemical shielding surfaces (ICSSs)<sup>54,55</sup> were generated with the Multiwfn 3.7 code.<sup>56</sup> The UV-vis and PES spectra were simulated using the time-dependent TD-DFT-PBE0 approach.<sup>57</sup>

## 3. Results and discussions

### 3.1 Structures and stabilities

We start from  $Ta_2B_7^+$ , the smallest di-metal-doped Ta-B complex concerned in this work. Extensive GM searches

indicate that inverse sandwich  $D_{7h}$   $Ta_2B_7^+$  (1,  $^1A_1$ ) is the deep-lying GM of the monocation which lies 1.58 eV lower than the second lowest-lying isomer  $C_{2v}$   $Ta_2B_7^+$  ( $^1A_1$ ) at CCSD(T) level (Fig. S1†), with the large HOMO-LUMO gap of  $\Delta E_{\text{gap}} = 3.77$  eV at PBE0. The monocation contains a perfect  $B_7$  ring sandwiched between two Ta atoms along the  $C_7$  molecular axis at the two ends (similar to the experimentally observed inverse sandwich  $D_{6h}$   $Ta_2B_6$  which has a perfect  $B_6$  ring sandwiched between two Ta atoms<sup>24</sup>), with the B-B bond length of  $r_{B-B} = 1.54$  Å, Ta-B distance of  $r_{Ta-B} = 2.28$  Å, and Ta-Ta distance of  $r_{Ta-Ta} = 2.86$  Å (which is obviously larger than the proposed Ta-Ta single bond length of 2.46 Å<sup>58</sup>). With one more B atom added in, the perfect inverse sandwich  $D_{8h}$   $Ta_2B_8$  (2,  $^1A_{1g}$ ) is achieved which is the deep-lying GM of the neutral lying 0.62 eV lower in energy than the second lowest-lying isomer  $C_s$   $Ta_2B_8$  ( $^1A'$ ) at CCSD(T) (Fig. S2†). It encompasses a perfect  $B_8$  ring sandwiched between two Ta atoms along the  $C_8$  molecular axis at the two ends, with the HOMO-LUMO gap of  $\Delta E_{\text{gap}} = 2.15$  eV at PBE0. With a  $B_8$  octagon as the ligand, the Ta-Ta distance in  $Ta_2B_8$  (2) is effectively shortened to  $r_{Ta-Ta} = 2.52$  Å which is close to the proposed average Ta-Ta single bond length.<sup>58</sup> The highly stable inverse sandwich  $Ta_2B_7^+$  (1) and  $Ta_2B_8$  (2) may serve as building blocks to form tri-metal-doped Ta-B complexes, similar to the situation in the experimentally observed triple-decker  $C_{2v}$   $La_3B_{14}^-$  (28) and spherical trihedral  $D_{3h}$   $La_3B_{18}^-$ .<sup>29</sup>

Following the direction, we obtained the lowest-lying  $C_{2v}$   $Ta_3B_{10}^+$  ( $^1A_1$ ) for  $Ta_3B_{10}^+$ ,  $C_s$   $Ta_3B_{11}^-$  ( $^1A'$ ) for  $Ta_3B_{11}^-$ , and  $C_s$   $Ta_3B_{11}^-$  ( $^2A'$ ) for  $Ta_3B_{11}^-$  which all possess incomplete spherical-trihedral structures with one edge broken (Fig. S3†). The smallest perfect spherical trihedron was achieved at  $D_{3h}$   $Ta_3B_{12}^-$  (3,  $^1A_1$ ) which, as the GM of the monoanion, lies 0.24 eV lower than the second lowest-lying  $C_{2v}$   $Ta_3B_{12}^-$  ( $^1A_1$ ) and 1.06 eV lower than the third lowest-lying  $C_s$   $Ta_3B_{12}^-$  ( $^1A'$ ) (which both belong to metallo-borospherenes) at the most reliable CCSD(T) level (Fig. S4†). As shown in Fig. 1,  $Ta_3B_{12}^-$  (3) contains three equivalent octa-coordinate Ta centres as integral parts of the cage surface coordinated in three equivalent  $\eta^8-B_8$  rings which share two eclipsed equilateral  $B_3$  triangles at the top and bottom interconnected by three  $B_2$  units on the waist. It has the calculated B-B bond lengths of  $r_{B-B} = 1.58-1.74$  Å, Ta-B coordination distances of  $r_{Ta-B} = 2.26-2.27$  Å, and elongated Ta-Ta distances

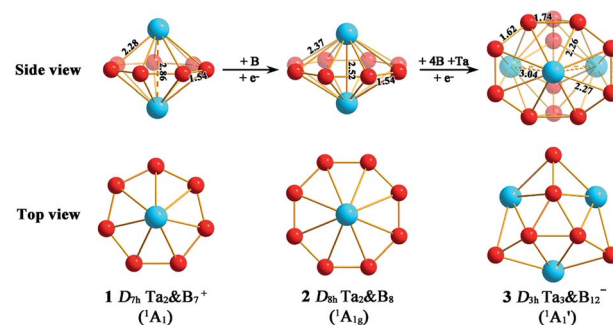


Fig. 1 Optimized structures of  $D_{7h}$   $Ta_2B_7^+$  (1),  $D_{8h}$   $Ta_2B_8$  (2), and  $D_{3h}$   $Ta_3B_{12}^-$  (3) at PBE0//B/aug-cc-pVTZ//Ta/Stuttgart+2f1g level, with bond lengths indicated in Å.



of  $r_{\text{Ta-Ta}} = 3.04 \text{ \AA}$ , respectively, with the large HOMO( $e''$ )-LOMO( $e'$ ) gap of  $\Delta E_{\text{gap}} = 2.50 \text{ eV}$  at PBE0 which is comparable with the corresponding value of  $2.70 \text{ eV}$  calculated for the experimentally observed  $D_{3h} \text{ La}_3\text{B}_{18}^-$  (29) at the same theoretical level.  $\text{Ta}_3\text{B}_{12}^-$  (3) can be constructed from  $\text{Ta}_2\text{B}_8$  (2) by adding one  $\text{B}_4$  edge ( $\text{>B-B-B-<}$ ) perpendicular to the  $\text{B}_8$  ring in the front and one Ta atom coordinated to the newly formed  $\text{B}_8$  ring, forming three interconnected  $\text{Ta}_2\text{B}_8$  inverse sandwiches around the  $C_3$  main molecular axis (Fig. 1). In comparison with  $D_{3h} \text{ Ln}_3\text{B}_{18}^-$  ( $\text{Ln} = \text{La, Tb}$ ) which possess a perfect cage-like  $D_{3h} \text{ B}_{18}$  ligand with three equivalent  $\eta^{10}\text{-B}_{10}$  decagons sharing two eclipsed  $\text{B}_6$  triangles at the top and bottom interconnected by three  $\text{B}_2$  units on the waist,<sup>29</sup>  $\text{Ta}_3\text{B}_{12}^-$  (3) has a perfect cage-like  $D_{3h} \text{ B}_{12}$  ligand with three equivalent  $\eta^8\text{-B}_8$  octagons sharing two eclipsed  $\text{B}_3$  triangles at the top and bottom interconnected by three  $\text{B}_2$  units on the waist.  $\text{Ta}_3\text{B}_{12}^-$  (3) has the same symmetry ( $D_{3h}$ ) as  $\text{Ln}_3\text{B}_{18}^-$ , but smaller in size with six less B atoms in the ligand. Such a structural change can be understood based on the fact that Ta ( $[\text{Xe}]5d^36s^2$ ) has a smaller atomic radius ( $1.46 \text{ \AA}$ ) than that ( $1.83 \text{ \AA}$ ) of La ( $[\text{Xe}]5d^16s^2$ ),<sup>59</sup> but possesses two more 5d valence electrons than the latter. The Ta centres appear to have the right atomic radii and electronic configurations to match the  $D_{3h} \text{ B}_{12}$  ligand both electronically and geometrically.  $\text{Ta}_3\text{B}_{12}^-$  (3) is therefore the smallest metallo-borospherene reported to date. Perfect spherical trihedral  $D_{3h} \text{ Nb}_3\text{B}_{12}^-$  and  $D_{3h} \text{ V}_3\text{B}_{12}^-$  also appear to be true minima of the systems at both PBE0 and BP86 levels (Fig. S5<sup>†</sup>), with the HOMO-LUMO gaps of  $\Delta E_{\text{gap}} = 2.59$  and  $2.67 \text{ eV}$  at PBE0, respectively.

Extensive MD simulations (Fig. S6<sup>†</sup>) indicate that  $\text{Ta}_2\text{B}_7^+$  (1),  $\text{Ta}_2\text{B}_8$  (2), and  $\text{Ta}_3\text{B}_{12}^-$  (3) are dynamically stable at 1200 K, 700 K, and 1200 K, with the small calculated average root-mean-square-deviations of  $\text{RMSD} = 0.11, 0.10,$  and  $0.11 \text{ \AA}$  and maximum bond length deviations of  $\text{MAXD} = 0.27, 0.24,$  and  $0.29 \text{ \AA}$ , respectively. No high-lying isomers were observed during the MD simulation. Ta-B complexes with larger HOMO-LUMO energy gaps appear to be dynamically more stable than the ones with narrower energy gaps.

### 3.2 Natural orbital and bonding analyses

The high stabilities of these high-symmetry complexes originate from their unique electronic structures and bonding patterns. Detailed natural bonding orbital (NBO) analyses show that the Ta centres in  $\text{Ta}_2\text{B}_7^+$  (1),  $\text{Ta}_2\text{B}_8$  (2), and  $\text{Ta}_3\text{B}_{12}^-$  (3) possess the electronic configurations of Ta  $[\text{Xe}]6s^{0.21}5d^{3.46}$ , Ta  $[\text{Xe}]6s^{0.22}5d^{3.64}$ , and Ta  $[\text{Xe}]6s^{0.24}5d^{3.72}$ , natural atomic charges of  $q_{\text{Ta}} = +1.34|e|, +1.12|e|$  and  $+1.01|e|$ , and total Wiberg bond indexes of  $\text{WBI}_{\text{Ta-B}} = 4.85, 4.80,$  and  $5.07$ , respectively, indicating that each Ta centre in these complexes donates its  $6s^2$  electrons almost completely to the  $\text{B}_n$  ligand ( $n = 7, 8, 12$ ), while, in return, accepts roughly one electron in its partially filled 5d orbitals from the  $\text{B}_n$  ligands *via*  $p \rightarrow d$  back-donations. The formations of effective Ta-B coordination interactions in 1-3 are strongly supported by the calculated Ta-B bond orders of  $\text{WBI}_{\text{Ta-B}} = 0.59, 0.40,$  and  $0.50\text{--}0.53$  (Ta-B interactions within  $\text{TaB}_7$  or  $\text{TaB}_8$  pyramids) which appear to be systematically higher than the typical Cr-C coordination bond orders of

$\text{WBI}_{\text{Cr-C}} = 0.34$  in  $D_{6h} \text{ Cr}(\text{C}_6\text{H}_6)_2$ . As mentioned above, a Ta centre in  $\text{Ta}_3\text{B}_{12}^-$  (3) has the total bond order of  $\text{WBI}_{\text{Ta}} = 5.07$  which is also obviously higher than the corresponding value of  $\text{WBI}_{\text{Cr}} = 4.12$  calculated for Cr in  $D_{6h} \text{ Cr}(\text{C}_6\text{H}_6)_2$ .

Detailed AdNDP bonding analyses unveil both the localized and delocalized bonds of the concerned systems. As shown in Fig. 2a,  $\text{Ta}_2\text{B}_8$  (2) possesses 8  $2c\text{--}2e$  B-B  $\sigma$  bonds on the periphery of the  $\eta^8\text{-B}_8$  ligand with the occupation numbers of  $\text{ON} = 1.82|e|$  and 1  $2c\text{--}2e$  Ta-Ta  $\sigma$  bond between the two Ta centres with  $\text{ON} = 2.00|e|$  in the first row. The remaining 16 valence electrons form 8 totally delocalized  $10c\text{--}2e$  coordination bonds between the  $\eta^8\text{-B}_8$  ligand and two Ta coordination centres with  $\text{ON} = 2.00|e|$ , including 3  $10c\text{--}2e$   $\sigma$  bonds in the second row, 3  $10c\text{--}2e$   $\pi$  bonds in the third row, and 2  $10c\text{--}2e$  (p-d)  $\delta$  bonding interactions in the fourth row. Both the

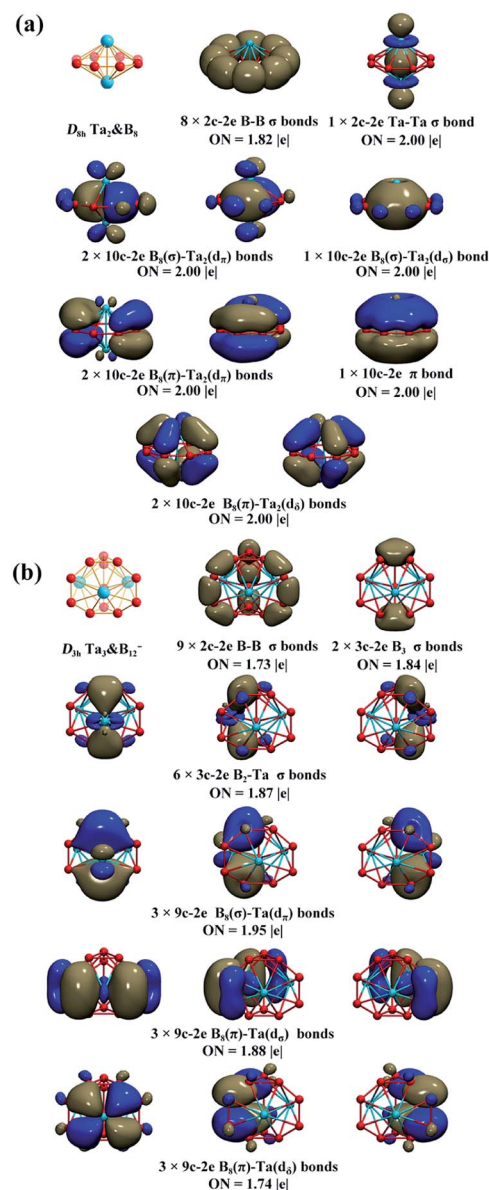


Fig. 2 AdNDP bonding patterns of (a)  $D_{8h} \text{ Ta}_2\text{B}_8$  (2) and (b)  $D_{3h} \text{ Ta}_3\text{B}_{12}^-$  (3), with the occupation numbers (ON) indicated.



delocalized 6e  $\sigma$ -system and delocalized 6e  $\pi$ -system match the  $4n + 2$  aromatic rule ( $n = 1$ ) and together they render  $\sigma + \pi$  dual aromaticity to  $\text{Ta}_2\text{B}_8$  (2). Similarly, both the experimentally observed  $D_{6h}$   $\text{Ta}_2\text{B}_6$  (ref. 25) and  $D_{7h}$   $\text{Ta}_2\text{B}_7^+$  (1) are  $\sigma + \pi$  doubly aromatic in nature, as clearly indicated in their canonical molecular orbitals (CMOs) depicted in Fig. S7.†

The AdNDP bonding pattern of spherical trihedral  $\text{Ta}_3\text{B}_{12}^-$  (3) (Fig. 2b) exhibits certain similarity with that of the inverse sandwich  $\text{Ta}_2\text{B}_8$  (2), but it is more complex and intriguing.  $\text{Ta}_3\text{B}_{12}^-$  (3) possesses 9 localized 2c–2e  $\sigma$  B–B bonds in the three  $\text{B}_2$  units and between the  $\text{B}_2$  units and the six apexes of the two  $\text{B}_3$  triangles and 2 equivalent 3c–2e  $\sigma$  bonds on the two  $\text{B}_3$  triangles at the top and bottom in the first row and 6 equivalent 3c–2e  $\text{B}_2$ –Ta  $\sigma$  bonds between the three Ta atoms and the two  $\text{B}_3$  triangles at the top and bottom in the second row. The remaining 18 valence electrons form 9 delocalized 9c–2e bonds evenly distributed on three equivalent  $C_{2v}$   $\text{TaB}_8$  octagonal pyramids (which are similar to the experimentally observed  $C_{8v}$   $\text{TaB}_8^-$  octagonal pyramid<sup>17</sup>) around the  $C_3$  main molecular axis, including 3 equivalent 9c–2e  $\text{B}_8(\sigma)$ –Ta( $d_\pi$ ) bonds in the third row, 3 equivalent 9c–2e  $\text{B}_8(\pi)$ –Ta( $d_\sigma$ ) bonds in the fourth row, and 3 equivalent  $\text{B}_8(\pi)$ –Ta( $d_\delta$ ) bonds in the fifth row. Each  $\text{TaB}_8$  octagonal pyramid thus possesses 1 9c–2e  $\text{B}_8(\sigma)$ –Ta( $d_\pi$ ) bond, 1 9c–2e  $\text{B}_8(\pi)$ –Ta( $d_\sigma$ ) bond, and 1  $\text{B}_8(\pi)$ –Ta( $d_\delta$ ) bond. Overall, the  $\text{Ta}_3\text{B}_{12}^-$  (3) spherical trihedron has 3 equivalent (d–p) $\sigma$  bonds, 3 equivalent (d–p) $\pi$  bonds, and 3 equivalent (d–p) $\delta$  bonds evenly distributed on three equivalent  $\text{TaB}_8$  octagonal pyramids around the  $C_3$  molecular axis, forming one delocalized 6e  $\sigma$ -system, one delocalized 6e  $\pi$ -system, and one delocalized 6e  $\delta$ -system on the cage surface each matching the  $4n + 2$  rule ( $n = 1$ ) independently. Such a delocalized bonding pattern renders  $\sigma + \pi + \delta$  triple aromaticity to the smallest metallo-borospherene of  $\text{Ta}_3\text{B}_{12}^-$  (3) which is a highly stable  $D_{3h}$  spherical trihedron with 18 delocalized electrons evenly distributed on the cage surface.<sup>60</sup>

The aromatic nature of  $\text{Ta}_2\text{B}_7^+$  (1),  $\text{Ta}_2\text{B}_8$  (2), and  $\text{Ta}_3\text{B}_{12}^-$  (3) is further evidenced by their calculated nucleus-independent chemical shift (NICS) values of NICS = –110.5, –101.9, and –86.6 ppm at the geometrical centres, respectively. Based on the calculated NICS-ZZ components, Fig. 3 plots their iso-chemical-shielding surfaces<sup>54,55</sup> with Z-axis parallel to the designated  $C_7$ ,  $C_8$ , or  $C_2$  molecular axes to illuminate the chemical shielding around the  $\text{TaB}_7$  or  $\text{TaB}_8$  pyramids in these complexes. Obviously, the space inside the spherical trihedron surrounded by the delocalized Ta– $\text{B}_n$  coordination bonds in horizontal direction or within about 1.0 Å above the Ta centres in vertical direction belong to chemical shielding regions (highlighted in yellow) with negative NICS-ZZ values, indicating that the aromatic contribution mainly comes from Ta(5d)–B(2p) coordination interactions between the Ta centres and  $\text{B}_n$  ligands around them ( $n = 7$  or 8), while the chemical de-shielding areas (highlighted in green) with positive NICS values are located outside the  $\text{B}_n$  ring in horizontal direction. The ICSSs of these complexes appear to be analogous to that of the prototypical aromatic benzene.<sup>54–56</sup>

Fig. S8† depicts the corresponding ring current maps of  $\text{Ta}_2\text{B}_7^+$  (1),  $\text{Ta}_2\text{B}_8$  (2), and  $\text{Ta}_3\text{B}_{12}^-$  (3). Consistent magnetic

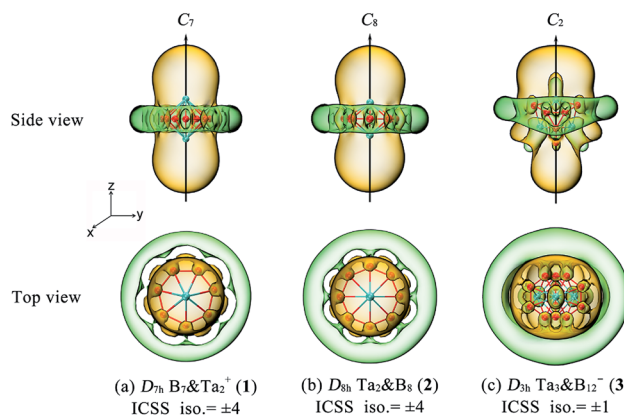


Fig. 3 Calculated iso-chemical shielding surfaces (ICSSs) of (a)  $\text{Ta}_2\text{B}_7^+$  (1), (b)  $\text{Ta}_2\text{B}_8$  (2), and (c)  $\text{Ta}_3\text{B}_{12}^-$  (3), with the corresponding NICS-ZZ components indicated. The  $C_7$  axis of  $\text{Ta}_2\text{B}_7^+$  (1),  $C_8$  axis of  $\text{Ta}_2\text{B}_8$  (2), and  $C_2$  axis of  $\text{Ta}_3\text{B}_{12}^-$  (3) are designated as z axis in vertical direction to compare the shielding effects around the  $\text{TaB}_n$  pyramids ( $n = 7, 8$ ). Yellow regions stand for chemical shielding areas, while green areas represent chemical de-shielding areas.

responses occur in 1, 2, and 3 in an external magnetic field in the vertical direction parallel to the assigned molecular axes, irrespective of the electron type, similar to the situations in both benzene<sup>52,53</sup> and double-ring tubular  $\text{B}_{20}$  (61) which are known to possess typical planar or tubular aromaticity. Such diatropic ring currents well support the aromatic nature of these Ta-doped boron complexes.

### 3.3 Simulated IR, Raman, and PE spectra of $\text{Ta}_3\text{B}_{12}^-$ (3)

We computationally simulate the IR, Raman, and UV-vis or PES spectra of  $\text{Ta}_2\text{B}_7^+$  (1),  $\text{Ta}_2\text{B}_8$  (2), and  $\text{Ta}_3\text{B}_{12}^-$  (3) at PBE0 level to facilitate their future spectral characterizations. PE measurements and infrared photodissociation (IR-PD) spectra in combination with first-principles theory calculations have proven to be powerful approaches in characterizing novel clusters in gas phases.<sup>3–7,17–28,62</sup> As shown in Fig. 4, the high-symmetry  $\text{Ta}_3\text{B}_{12}^-$  (3) exhibits relatively simple IR and Raman spectral patterns, with the major IR active peaks at 507 ( $e'$ ), 559 ( $e'$ ), 668 ( $a_2''$ ), and 881 ( $e'$ )  $\text{cm}^{-1}$  (Fig. 4a) and main Raman spectral features at 209 ( $a_1'$ ), 881 ( $e'$ ), 998 ( $e''$ ), and 1201 ( $a_1'$ )  $\text{cm}^{-1}$  (Fig. 4b), respectively. The first Raman active symmetrical vibrational mode ( $a_1'$ ) at 209  $\text{cm}^{-1}$  corresponds to typical “radial breathing mode” (RBM) of the metallo-borospherene which may be used to characterize the hollow structures of single-walled boron nanoclusters in experiments.<sup>63</sup>

The calculated PE spectrum of  $\text{Ta}_3\text{B}_{12}^-$  (3) in Fig. 4c exhibits major spectral features at 2.95 ( ${}^2E''$ ), 3.17 ( ${}^2A_1'$ ), 3.66 ( ${}^2A_2''$ ), 3.98 ( ${}^2E'$ ), 4.17 ( ${}^2A_1''$ ), 5.32 ( ${}^2E'$ ), 5.68 ( ${}^2E'$ ), and 5.98 ( ${}^2A_2''$ ), respectively, corresponding to vertical electronic transitions from the ground state of the anion ( ${}^1A_1'$ ) to the excited states of the neutral at the ground-state geometry of the anion. The open-shell neutral  $\text{Ta}_3\text{B}_{12}$  has a slightly distorted  $C_{2v}$   $\text{Ta}_3\text{B}_{12}$  ( ${}^2A_2$ ) ground-state structure due to Jahn–Teller effect, with the calculated electron affinity of EA = 2.87 eV. The simulated IR, Raman, and UV-vis spectra of  $\text{Ta}_2\text{B}_7^+$  (1) and  $\text{Ta}_2\text{B}_8$  (2) are depicted in Fig. S9.†



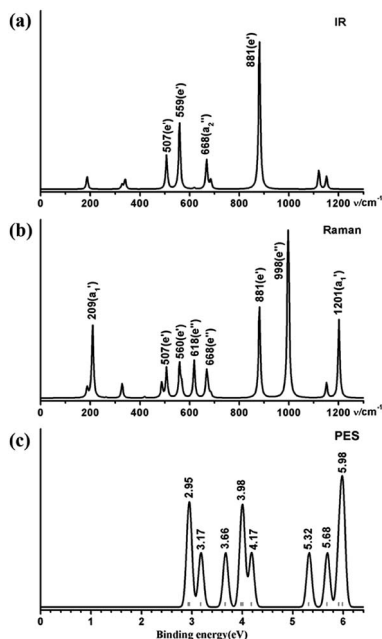


Fig. 4 Simulated (a) IR, (b) Raman, and (c) PES spectra of  $D_{3h}$   $Ta_3B_{12}^-$  (3) at PBE0//B/aug-cc-pVTZ//Ta/Stuttgart+2f1g level.

## 4. Conclusions

Extensive first-principles theory calculations performed in this work indicate a structural transition from perfect inverse sandwich  $D_{7h}$   $Ta_2B_7^+$  (1) and  $D_{8h}$   $Ta_2B_8$  (2) to the smallest metallo-borospherene  $D_{3h}$   $Ta_3B_{12}^-$  (3). As the first transition-metal-doped boron complex reported to date with  $\sigma + \pi + \delta$  triple aromaticity,  $Ta_3B_{12}^-$  (3) possesses three octa-coordinate Ta centres as integral parts of the cage surface coordinated in three equivalent  $\eta^8-B_8$  octagons. The results obtained in this work suggest that a large family of coordination-stabilized multi-TM-doped  $TM_mB_n$  metallo-borospherenes with tunable magnetic and electronic properties may exist in experiments in which the transition metal dopants and  $B_n$  ligands match both geometrically and electronically.

## Conflicts of interest

There are no conflicts to declare.

## Acknowledgements

The work was supported by the National Natural Science Foundation of China (21720102006 and 21973057 to S.-D. Li).

## Notes and references

- 1 W. N. Lipscomb, *Science*, 1977, **196**, 1047.
- 2 F. A. Cotton, G. Wilkinson, C. A. Murillo, and M. Bochmann, *Advanced Inorganic Chemistry*, Wiley, New York, 6th edn, 1999.
- 3 L. S. Wang, *Int. Rev. Phys. Chem.*, 2016, **35**, 69.

- 4 T. Jian, X. N. Chen, S. D. Li, A. I. Boldyrev, J. Li and L. S. Wang, *Chem. Soc. Rev.*, 2019, **48**, 3550.
- 5 H. J. Zhai, Y. F. Zhao, W. L. Li, Q. Chen, H. Bai, H. S. Hu, Z. A. Piazza, W. J. Tian, H. G. Lu, Y. B. Wu, Y. W. Mu, G. F. Wei, Z. P. Liu, J. Li, S. D. Li and L. S. Wang, *Nat. Chem.*, 2014, **6**, 727.
- 6 Q. Chen, W. L. Li, Y. F. Zhao, S. Y. Zhang, H. S. Hu, H. Bai, H. R. Li, W. J. Tian, H. G. Lu, H. J. Zhai, S. D. Li, J. Li and L. S. Wang, *ACS Nano*, 2015, **9**, 754.
- 7 Q. Chen, S. Y. Zhang, H. Bai, W. J. Tian, T. Gao, H. R. Li, C. Q. Miao, Y. W. Mu, H. G. Lu, H. J. Zhai and S. D. Li, *Angew. Chem., Int. Ed.*, 2015, **54**, 8160.
- 8 Q. Chen, H. R. Li, C. Q. Miao, Y. J. Wang, H. G. Lu, Y. W. Mu, G. M. Ren, H. J. Zhai and S. D. Li, *Phys. Chem. Chem. Phys.*, 2016, **18**, 11610.
- 9 W. J. Tian, Q. Chen, H. R. Li, M. Yan, Y. W. Mu, H. G. Lu, H. J. Zhai and S. D. Li, *Phys. Chem. Chem. Phys.*, 2016, **18**, 9922.
- 10 Q. Chen, H. R. Li, W. J. Tian, H. G. Lu, H. J. Zhai and S. D. Li, *Phys. Chem. Chem. Phys.*, 2016, **18**, 14186.
- 11 Y. J. Wang, Y. F. Zhao, W. L. Li, T. Jian, Q. Chen, X. R. You, T. Ou, X. Y. Zhao, H. J. Zhai, S. D. Li, J. Li and L. S. Wang, *J. Chem. Phys.*, 2016, **144**, 064307.
- 12 H. R. Li, T. Jian, W. L. Li, C. Q. Miao, Y. J. Wang, Q. Chen, X. M. Luo, K. Wang, H. J. Zhai, S. D. Li and L. S. Wang, *Phys. Chem. Chem. Phys.*, 2016, **18**, 29147.
- 13 L. Pei, H. R. Li, M. Yan, Q. Chen, Y. W. Mu, H. G. Lu, Y. B. Wu and S. D. Li, *Phys. Chem. Chem. Phys.*, 2018, **20**, 15330.
- 14 L. Pei, M. Yan, X. Y. Zhao, Y. W. Mu, H. G. Lu, Y. B. Wu and S. D. Li, *RSC Adv.*, 2020, **10**, 10129.
- 15 H. Liu, Q. Chen, H. R. Li, X. Y. Zhao, X. X. Tian, Y. W. Mu, H. G. Lu and S. D. Li, *Phys. Chem. Chem. Phys.*, 2018, **20**, 15344.
- 16 X. Y. Zhao, Q. Chen, H. R. Li, Y. W. Mu, H. G. Lu and S. D. Li, *Phys. Chem. Chem. Phys.*, 2017, **19**, 10998.
- 17 W. L. Li, A. S. Ivanov, J. Federič, C. Romanescu, I. Čerušák, A. I. Boldyrev and L. S. Wang, *J. Chem. Phys.*, 2013, **139**, 104312.
- 18 C. Romanescu, T. R. Galeev, W. L. Li, A. I. Boldyrev and L. S. Wang, *J. Chem. Phys.*, 2013, **138**, 134315.
- 19 T. R. Galeev, C. Romanescu, W. L. Li, L. S. Wang and A. I. Boldyrev, *Angew. Chem., Int. Ed.*, 2012, **51**, 2101.
- 20 B. L. Chen, W. G. Sun, X. Y. Kuang, C. Lu, X. X. Xia, H. X. Shi and G. Maroulis, *Inorg. Chem.*, 2018, **57**, 343.
- 21 I. A. Popov, T. Jian, G. V. Lopez, A. I. Boldyrev and L. S. Wang, *Nat. Commun.*, 2015, **6**, 8654.
- 22 T. Jian, W. L. Li, X. Chen, T. T. Chen, G. V. Lopez, J. Li and L. S. Wang, *Chem. Sci.*, 2016, **7**, 7020.
- 23 W. L. Li, T. Jian, X. Chen, H. R. Li, T. T. Chen, X. M. Luo, S. D. Li, J. Li and L. S. Wang, *Chem. Commun.*, 2017, **53**, 1587.
- 24 M. Yan, H. R. Li, X. Y. Zhao, X. Q. Lu, Y. W. Mu, H. G. Lu and S. D. Li, *J. Comput. Chem.*, 2019, **40**, 966.
- 25 W. L. Li, L. Xie, T. Jian, C. Romanescu, X. Huang and L. S. Wang, *Angew. Chem.*, 2014, **126**, 1312.
- 26 W. L. Li, T. T. Chen, D. H. Xing, X. Chen, J. Li and L. S. Wang, *Proc. Natl. Acad. Sci. U. S. A.*, 2018, **115**, E6972.



## Paper

- 27 X. Q. Lu, Q. Chen, X. X. Tian, Y. W. Mu, H. G. Lu and S. D. Li, *Nanoscale*, 2019, **11**, 21311.
- 28 T. T. Chen, W. L. Li, W. J. Chen, J. Li and L. S. Wang, *Chem. Commun.*, 2019, **55**, 7864.
- 29 T. T. Chen, W. L. Li, W. J. Chen, X. H. Yu, X. R. Dong, J. Li and L. S. Wang, *Nat. Commun.*, 2020, **11**, 2766.
- 30 H. Bai, Q. Chen, H. J. Zhai and S. D. Li, *Angew. Chem., Int. Ed.*, 2015, **54**, 941.
- 31 H. R. Li, X. X. Tian, X. M. Luo, M. Yan, Y. W. Mu, H. G. Lu and S. D. Li, *Sci. Rep.*, 2017, **7**, 5701.
- 32 Y. F. Zhao, X. Chen and J. Li, *Nano Res.*, 2017, **10**, 3407.
- 33 X. Chen, Y. F. Zhao, L. S. Wang and J. Li, *Comput. Theor. Chem.*, 2017, **1107**, 57.
- 34 D. J. Wales and J. P. Doye, *J. Phys. Chem. A*, 1997, **101**, 5111.
- 35 J. P. Perdew, K. Burke and M. Ernzerhof, *Phys. Rev. Lett.*, 1996, **77**, 3865.
- 36 C. Adamo and V. Barone, *J. Chem. Phys.*, 1999, **110**, 6158.
- 37 D. Feller, *J. Comput. Chem.*, 1996, **17**, 1571.
- 38 D. Andrae, U. Häußermann, M. Dolg, H. Stoll and H. Preuß, *Theor. Chim. Acta*, 1990, **77**, 123.
- 39 J. M. L. Martin and A. Sundermann, *J. Chem. Phys.*, 2001, **114**, 3408.
- 40 M. J. Frisch, *et al.*, *Gaussian 16, Revision A.03*, Gaussian Inc., Wallingford, CT, 2016.
- 41 A. D. Becke, *Phys. Rev. A: At., Mol., Opt. Phys.*, 1988, **38**, 3098.
- 42 J. P. Perdew, *Phys. Rev. B: Condens. Matter Mater. Phys.*, 1986, **33**, 8822.
- 43 T. H. Dunning Jr, *J. Chem. Phys.*, 1989, **90**, 1007.
- 44 R. A. Kendall, T. H. Dunning Jr and R. J. Harrison, *J. Chem. Phys.*, 1992, **96**, 6796.
- 45 J. Čížek, *Adv. Chem. Phys.*, 1969, **14**, 35.
- 46 G. D. Purvis and R. J. Bartlett, *J. Chem. Phys.*, 1982, **76**, 1910.
- 47 K. Raghavachari, G. W. Trucks, J. A. Pople and M. Head-Gordon, *Chem. Phys. Lett.*, 1989, **157**, 479.
- 48 P. E. D. Glendening, J. K. Badenhoop, A. E. Reed, J. E. Carpenter, J. A. Bohmann, C. M. Morales, C. R. Landis and F. Weinhold, *NBO 6.0*, Theoretical Chemistry Institute, University of Wisconsin, Madison, 2013.
- 49 D. Y. Zubarev and A. I. Boldyrev, *Phys. Chem. Chem. Phys.*, 2008, **10**, 5207.
- 50 N. V. Tkachenko and A. I. Boldyrev, *Phys. Chem. Chem. Phys.*, 2019, **21**, 9590.
- 51 J. VandeVondele, M. Krack, F. Mohamed, M. Parrinello, T. Chassaing and J. Hutter, *Comput. Phys. Commun.*, 2005, **167**, 103.
- 52 D. Geuenich, K. Hess, F. Köhler and R. Herges, *Chem. Rev.*, 2005, **105**, 3758.
- 53 Povray, *Persistence of vision raytracer, POV-Ray 3.7*, <http://www.povray.org/>.
- 54 S. Klod and E. Kleinpeter, *J. Chem. Soc., Perkin Trans. 2*, 2001, **2**, 1893.
- 55 E. Kleinpeter, S. Klod and A. Koch, *J. Mol. Struct.*, 2007, **811**, 45.
- 56 T. Lu and F. W. Chen, *J. Comput. Chem.*, 2012, **33**, 580.
- 57 R. Bauernschmitt and R. Ahlrichs, *Chem. Phys. Lett.*, 1996, **256**, 454.
- 58 P. Pykkö and M. Atsumi, *Chem.–Eur. J.*, 2009, **15**, 186.
- 59 J. A. Dean, *Lange's Hand book of Chemistry*, McGraw-Hill Book Co., 1999, Table 4.6.
- 60 A. Tlahuice-Flores and A. Muñoz-Castro, *Int. J. Quantum Chem.*, 2019, **119**, e25756.
- 61 M. P. Johansson, *J. Phys. Chem. C*, 2009, **113**, 524.
- 62 G. J. Wang, M. F. Zhou, J. T. Goettel, G. J. Schrobilgen, J. Su, J. Li, T. Schlöder and S. Riedel, *Nature*, 2014, **514**, 475.
- 63 D. Ciuparu, R. F. Klie, Y. Zhu and A. L. Pfeifferle, *J. Phys. Chem. B*, 2004, **108**, 3967.

